

J0526+5934: a peculiar ultra-short period double white dwarf

Alberto Rebassa-Mansergas^{1,2*}, Mark Hollands³, Steven G. Parsons³, Leandro G. Althaus^{4,5}, Ingrid Pelisoli⁶, Puji Irawati⁷, Roberto Raddi¹, Maria E. Camisassa¹, Santiago Torres^{1,2}

¹ Departament de Física, Universitat Politècnica de Catalunya, c/Esteve Terrades 5, 08860 Castelldefels, Spain

² Institute for Space Studies of Catalonia, c/Gran Capità 2–4, Edif. Nexus 104, 08034 Barcelona, Spain

³ Department of Physics and Astronomy, University of Sheffield, Sheffield, S3 7RH, UK

⁴ Facultad de Ciencias Astronómicas y Geofísicas, Universidad Nacional de La Plata, Paseo del Bosque s/n, 1900 La Plata, Argentina

⁵ Instituto de Astrofísica La Plata, UNLP-CONICET, Paseo del Bosque s/n, 1900 La Plata, Argentina

⁶ Department of Physics, University of Warwick, Coventry, CV4 7AL, UK

⁷ National Astronomical Research Institute of Thailand, 260 Moo 4, T. Donkaew, A. Maerim, Chiangmai, 50180 Thailand

Received ; accepted

ABSTRACT

Context. Ultra-short period compact binaries are important sources of gravitational waves, which include e.g. the progenitors of type Ia supernovae or the progenitors of merger episodes that may lead to massive and magnetic single white dwarfs. J0526+5934 is an unresolved compact binary star with an orbital period of 20.5 minutes that belongs to this category.

Aims. The visible component of J0526+5934 has been recently claimed to be a hot sub-dwarf star with a CO white dwarf companion. Our aim is to provide strong observational plus theoretical evidence that the primary star is rather an extremely-low mass white dwarf, although the hot subdwarf nature cannot be completely ruled out.

Methods. We analyse optical spectra together with time-series photometry of the visible component of J0526+5934 to constrain its orbital and stellar parameters. We also employ evolutionary sequences for low-mass white dwarfs to derive independent values of the primary mass.

Results. From the analysis of our observational data, we find a stellar mass for the primary star in J0526+5934 of $0.26 \pm 0.05 M_{\odot}$, which perfectly matches the $0.237 \pm 0.035 M_{\odot}$ independent measurement we derived from the theoretical evolutionary models. This value is considerably lower than the theoretically expected and generally observed mass range of hot subdwarf stars, but falls well within the mass limit values of extremely low-mass white dwarfs.

Conclusions. We conclude J0526+5934 is the fifth ultra-short period detached double white dwarf currently known.

Key words. (Stars:) white dwarfs; (Stars:) binaries (including multiple): close

1. Introduction

Together with low-mass main sequence stars, white dwarfs are the most common objects in our Galaxy. Indeed, over 95% of main sequence stars will become, or have already turned into, white dwarfs (Althaus et al. 2010). That is, after all nuclear evolutionary phases take place, only the hot Earth-sized core of the star remains, typically with a mass of $\approx 0.6 M_{\odot}$ (Hollands et al. 2018; Kilic et al. 2020; McCleery et al. 2020; Jiménez-Esteban et al. 2023; O’Brien et al. 2024). Once they are formed, these compact objects cool down over periods of time that are larger than the Hubble time, a cooling process that is relatively well understood (Blouin et al. 2019; Bauer et al. 2020; Camisassa et al. 2016, 2019, 2023). As a consequence, white dwarfs are very valuable tools that can be used as cosmochronometers to e.g. place constraints of the ages of open and globular clusters (e.g. García-Berro et al. 2010; Jeffery et al. 2011; Torres et al. 2015) as well as the age of the Galactic disk (e.g. García-Berro et al. 1988; Oswalt et al. 1996) and halo (e.g. Kilic et al. 2020; Torres et al. 2021). If the white dwarfs are in wide-enough binary systems with main sequence companions (where no mass transfer episodes took place in the past), they can be used to provide ages for their companions to thus constrain e.g. the age-metallicity relation (Rebassa-Mansergas et al. 2016, 2021)

and the age-velocity dispersion relation (Raddi et al. 2022) of the Milky Way, or the age-activity-rotation relation of low-mass main sequence stars (Rebassa-Mansergas et al. 2013; Morgan et al. 2012; Skinner et al. 2017; Rebassa-Mansergas et al. 2023).

White dwarf binaries are also of extreme interest when the orbital separations are short, of the order of a few days or less. In these cases, the systems most likely formed via at least one common envelope evolution (Webbink 2008). For example, post-common envelope white dwarf-main sequence binaries have been proven to be very valuable to constrain current theories of common envelope evolution (Camacho et al. 2014; Cojocaru et al. 2017; Zorotovic & Schreiber 2022) and magnetic braking (Schreiber et al. 2010; Zorotovic et al. 2016), as well as to constrain the mass-radius relation of white dwarfs (Parsons et al. 2017), brown dwarfs (van Roestel et al. 2021), sub-dwarf stars (Rebassa-Mansergas et al. 2019a) and main sequence stars (Parsons et al. 2018) if they are eclipsing. One of the possible products of post-common envelope systems are double white dwarfs, considering that the main sequence companions have had time to evolve out of the main sequence, thus forcing the systems to enter a second common envelope phase. However, it is not clear yet whether or not double white dwarfs form through two episodes of common envelope (Nelemans & Tout 2005; van der Sluis et al. 2006), and an alternative scenario has been proposed that involves a first phase of stable but non-conservative mass trans-

* E-mail: alberto.rebassa@upc.edu

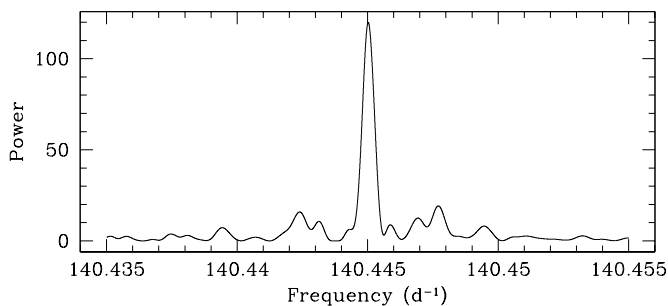


Fig. 1. Scargle periodogram of J0526+5934 resulting from our analysis of the ZTF data. The strongest peak corresponds to a period of ≈ 10 minutes, which is half the true orbital period.

fer followed by a common envelope episode (Woods et al. 2012; Ge et al. 2015; Schreiber et al. 2022). In any case, short-period double white dwarfs are important gravitational wave sources, which will be the dominant sources for the forthcoming Laser Interferometer Space Antenna (LISA) mission (Korol et al. 2018) and are also one of the favoured systems to produce type Ia supernovae (Whelan & Iben 1973; Iben & Tutukov 1984; Liu et al. 2018). Finding potential double-degenerate supernovae Ia progenitors is extremely challenging via optical spectroscopy, however they are expected to be found through their detection of gravitational waves (Rebassa-Mansergas et al. 2019b).

Currently, there are several hundred double white dwarfs known (Rebassa-Mansergas et al. 2017; Breedt et al. 2017; Maoz et al. 2018; Napiwotzki et al. 2020), many of which are eclipsing (Hallakoun et al. 2016; Parsons et al. 2020; Keller et al. 2022; Kosakowski et al. 2022; Munday et al. 2023). Of particular interest are those that contain an extremely low-mass (ELM) white dwarf ($\leq 0.3 M_{\odot}$). These objects cannot be formed in isolated evolution, and are believed to be formed as a result of a common-envelope phase or after an episode of stable Roche-lobe overflow (Istrate et al. 2016; Li et al. 2019). Most of the known objects belonging to this type have been identified thanks to the mining of the Sloan Digital Sky Survey spectroscopic data base (Gianninas et al. 2015; Bell et al. 2017; Brown et al. 2020, 2022). With the advent of the astrometric and photometric data provided by the *Gaia* satellite (Gaia Collaboration et al. 2018; Gaidos et al. 2023), many more ELM white dwarfs are being identified (Inight et al. 2021; Wang et al. 2022; Kosakowski et al. 2023a). We are currently in the process of building and characterising a volume-limited sample of ELM white dwarfs using *Gaia* plus follow-up spectroscopy (Pelisoli & Vos 2019). As a result of this endeavour, we have identified a peculiar ultra-short period (< 25 minutes) double white dwarf presumably containing an ELM white dwarf, which we present and analyse in detail in this work.

The structure of the paper is as follows. In Section 2 we introduce J0526+5934, the target of study. In Section 3 we describe our extensive follow-up campaign. The results, including our spectral and light-curve analysis, are presented in Section 4. We discuss our results in Section 5 and summarise and conclude the work in Section 6.

2. J0526+5934

Pelisoli & Vos (2019) identified J0526+5934 (RA = 81.54342°, DEC = 59.57926°; *Gaia* DR3 ID = 282679289838317184) as an ELM white dwarf candidate. Zwicky Transient Facility, ZTF (Masci et al. 2019; Dekany et al. 2020), photometry is available for this object and our analysis of the light-curve indicated a very

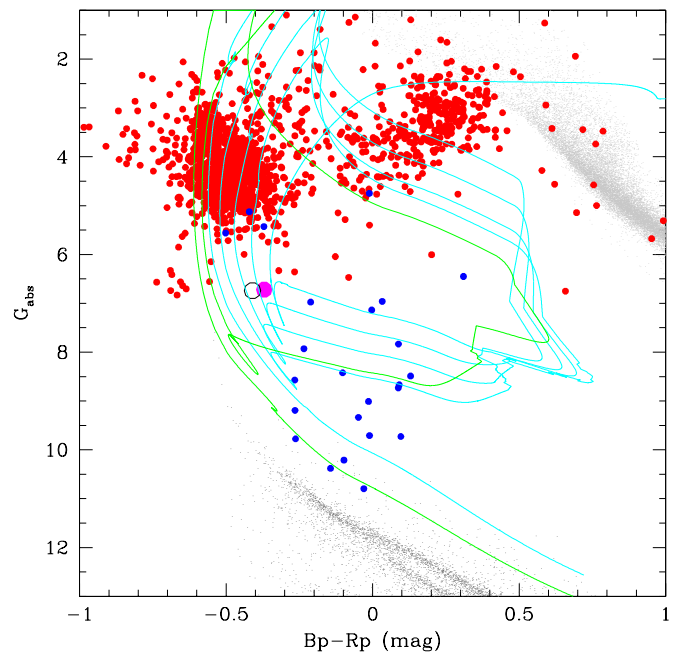


Fig. 2. Absolute magnitude-colour diagram of single white dwarfs (dark grey) and main sequence stars (light grey) within 100 pc from Jiménez-Esteban et al. (2023), hot subdwarf stars (red dots) from Geier (2020) and ELM white dwarfs (blue dots) from Brown et al. (2016); Kilic et al. (2017); Pelisoli et al. (2018). J0526+5934 (magenta solid dot) falls in the transition region between hot subdwarf stars and ELM white dwarfs. The black open circle represents the G_{abs} vs. $B_p - R_p$ that we obtain for J0526+5934 from our spectral modeling (Section 4.2), which is in good agreement with the *Gaia* observed value (magenta dot). All magnitudes have been dereddened using the extinction provided by the 3D maps of Lallement et al. (2014) except for J0526+5934 (in this case we used the reddening obtained from our analysis; Section 4.2) and only objects with positive parallaxes and relative errors below 10% have been considered. The cyan and green lines represent the evolutionary tracks for a $0.226 M_{\odot}$ and a $0.324 M_{\odot}$ ELM white dwarf, respectively, from Istrate et al. (2016).

short period of ≈ 10.25 minutes (see Figure 1). It is worth noting that the periodogram did not reveal any significant peak at double this value, which is, as we will see in the next section, the true orbital period (Ren et al. 2023).

The location of J0526+5934 in the *Gaia* colour magnitude diagram is far away from the typical white dwarf locus, and within the region of hydrogen shell flashes of proto ELM white dwarfs (see Figure 2). As it can be seen from the figure, J0526+5934 is also relatively close to the locus occupied by hot subdwarfs, and indeed it has been claimed that the visible component of this binary belongs to such category by Kosakowski et al. (2023b); Lin et al. (2023). This is mainly due to the fact that the authors measure a mass of $\approx 0.36 - 0.38 M_{\odot}$ for this compact object. In our analysis, as we will show in the forthcoming sections, we derive a mass for the visible component of $\approx 0.26 M_{\odot}$, which is fully and more compatible with the hypothesis that it is an ELM white dwarf. Although we find no robust evidence to rule out the subdwarf nature, we argue that the visible component of J0526+5934 is hence an ELM white dwarf and we treat it as such throughout the paper. We also assume that the unseen companion is another white dwarf (although the possibility exists that it belongs to a more exotic category such as a neutron star). Under these assumptions, J0526+5934 becomes the fifth ultra-short period detached double white dwarf known to

date, together with SDSS J065133.338+284423.37 (Brown et al. 2011, 12.7 minutes), ZTF J1539+5027 (Burdge et al. 2019a, 6.9 minutes), PTF J0533+0209 (Burdge et al. 2019b, 20.6 minutes) and ZTF J2243+5242 (Burdge et al. 2020, 8.8 minutes).

3. Observations

In this section we give details of the follow-up observations we carried out at the Telescopi Joan Oró, the Gran Telescopio Canarias and the Thai National Telescope.

3.1. Telescopi Joan Oró

The orbital period of J0526+5934 is too short for obtaining a high signal-to-noise spectrum in one single exposure without avoiding orbital smearing, given that it is quite faint ($G=17.5$ mag). For this reason, and with the aim of measuring an orbital period accurate enough to plan the spectroscopic observations, we first followed-up this object with the 0.8m Telescopi Joan Oró (TJO) located in the Montsec Observatory in Lleida, Spain.

We used the LAIA (Large Area Imager for Astronomy) instrument equipped with the 4k×4k Andor iKon XL CCD and the Johnson–Cousins V filter. The observations took place during the night of 2020/10/23 and lasted for a total of ≈ 5 hours. Individual exposure times were 130 seconds, reaching a signal-to-noise ratio of ≈ 50 for the target in each image. The readout time of the CCD is 8 seconds. The data were automatically reduced by the TJO internal pipeline, which also yields differential photometry for the target plus two comparison stars. The analysis of the TJO photometry resulted in an orbital period of 616.00 ± 0.66 seconds, in agreement with the ZTF measurement (Section 2; note that, in the same way as for the ZTF data, the strongest signal corresponded to half the true period).

3.2. Gran Telescopio Canarias

We obtained follow-up spectroscopy of J0526+5934 with the Gran Telescopio Canarias, GTC, at the Observatorio Roque de los Muchachos, La Palma. The telescope was equipped with the OSIRIS instrument, the 2000B grating and the 0.6'' slit. Thus, the spectra acquired covered the $\approx 3950\text{--}5700$ Å wavelength range at a resolving power of ≈ 2100 . The observations took place on 2022/11/26 and lasted ≈ 6.5 hours.

Given the short orbital period of J0526+5934, we avoided exposures longer than 1 minute, otherwise the spectra would have suffered from orbital smearing. We planned the observations under the assumption that the orbital period was the one we obtained from the analysis of the TJO data (Section 3.1). Thus, we aimed at obtaining 37 cycles of 12 short exposures of $27.93 + t_{\text{read}}$ seconds, where t_{read} is the CCD readout time (23.4 seconds, including also the setup for the next exposure) and $27.93 = (P_{\text{orb}}/12) - t_{\text{read}}$, where P_{orb} is the expected orbital period. As a consequence, this strategy would allow us to take 37 spectra at each 1/12th of the orbit in 6.5 hours, which we would then combine to obtain 12 spectra equally spread over the entire orbit. The orbital period uncertainty of ≈ 0.65 seconds (Section 3.1) implies a maximum drift of 24 seconds after the 6.5 hours, assuming the orbital period was 616 s. Given that the total time of 51.33 seconds (27.93 s of exposure plus 23.4 s of readout time) is longer than the maximum drift, this implies the 37 spectra at each 1/12th taken over the 6.5 hours can be combined without causing any smearing.

The observations were carried out following the above strategy and we reduced/calibrated the spectra using the *pamela* (Marsh 1989) and *MOLLY*¹ packages respectively. When combining the 37 spectra at each 1/12th of the orbit, we found the spectra displayed a double-lined profile of nearly identical lines. It was then that we realised these lines were exactly the same but shifted by the same amount both towards the blue and the red. In other words, the orbital period was twice the value we measured from the TJO data, 1232.00 ± 0.66 s, in agreement with the period reported by Ren et al. (2023); Kosakowski et al. (2023b); Lin et al. (2023), and we were sampling 24 points in the orbit rather than 12. As a consequence, we then combined the spectra at each 1/24th of the orbit. That is, we obtained 24 spectra of J0526+5934 equally spread over the orbit.

Note that since the orbital period is double what we expected, the maximum drift drops to 12 seconds for the length of the observations. As a consequence, our spectra do not suffer from orbital smearing.

3.3. Thai National Telescope

More follow-up photometric data of J0526+5934 were obtained with the 2.4m Thai National Telescope in Doi Inthanon, Thailand, using the ULTRASPEC instrument (Dhillon et al. 2014). The observations were conducted on 2020/03/29, 2020/12/10, and 2021/02/05 where we followed up the target for 2x the orbit, 3x the orbit, and 8x the orbit in each respective night. We opted to use the *KG5* filter ($u'+g'+r'$, Hardy et al. 2017) for all of our observations to optimise the signal-to-noise ratio. The data were taken in windowed mode with box sizes of $\approx 3\text{--}4$ arcminutes to ensure enough comparison stars within the field-of-view.

The data were then reduced using the HiPERCAM pipeline (Dhillon et al. 2007) to obtain the fluxes of J0526+5934 and nearby comparison stars. The signal-to-noise ratio from our data is 40 with 2.1s exposure time during the first observing night. The sky was clear in 2020/03/29 with seeing between 2–2.5. We got signal-to-noise $\lesssim 30$ in the second and the third runs due to weather conditions (intermittent clouds and seeing $\lesssim 1.5\text{--}3$). The exposure times used in both nights was ≈ 2 s.

4. Results

4.1. Radial velocities and radial velocity curve

In order to measure the radial velocities from the 24 GTC spectra (see Section 3.2), we first fitted the $H\beta$ absorption lines with a single Gaussian profile. We used these values to correct the spectra from the orbital motion, which we combined and run a model spectral fit (see details in Section 4.2) to obtain a preliminary best-fit model spectrum. In a second step, we used the *MOLLY* software to cross-correlate the normalised best-fit model spectrum to the 24 observed GTC spectra (also normalised). The cross-correlation technique yielded similar but more precise radial velocity values than those obtained from the Gaussian fits. The observed spectra were then corrected from the orbital motion using these refined velocities and the combined spectrum was then re-fitted to derive the effective temperature and surface gravity of the ELM white dwarf (see details in Section 4.2).

Once the radial velocities were obtained using the above procedure, we represented them as a function of orbital phase and fitted them with a sine curve. The radial velocity curve and the

¹ Developed by Tom Marsh and available at <http://deneb.astro.warwick.ac.uk/phsaap/software>.

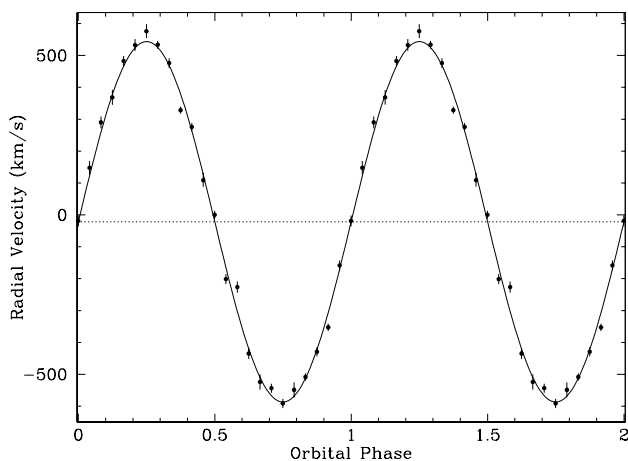


Fig. 3. Radial velocities of J0526+5934, representing the orbital motion of the ELM white dwarf (solid dots) as a function of orbital phase; where phase 0 indicates the time of inferior conjunction. The solid line is the best sine fit to the data and the horizontal dotted line indicates the systemic velocity.

corresponding sine fit can be seen in Figure 3. From this fit we obtained a semi-amplitude velocity of 565.2 ± 3.2 km/s for the brightest component and a systemic velocity of -21.6 ± 2.2 km/s.

4.2. Spectral model fit and mass of the visible component

To measure the atmospheric parameters of the ELM white dwarf, we performed a simultaneous fit to our coadded GTC spectra (Section 3.2) and the available photometry (*Gaia* DR3 and PanSTARRS DR1). For this purpose, we used the Koester 1D LTE white dwarf model atmosphere code (Koester 2010), assuming a negligible contribution from the white dwarf companion (see Section 4.4). As free parameters, we fitted the effective temperature (T_{eff}), the surface gravity ($\log g$), the helium abundance ($\log(\text{He}/\text{H})$), the solid angle of the star on the sky (Ω), the interstellar reddening ($E(B-V)$), and finally its rotational broadening ($v_{\text{eq}} \sin i$; where v_{eq} is the rotational velocity at the equator and i is the inclination).

Our fit consisted of an iterative χ^2 minimization against the spectrum and photometry. Rather than construct a grid of models around the approximate solution and interpolating, we recalculated our atmosphere code at each iteration in the fit, to ensure self-consistency. After computing the model at the start of each iteration, we convolved the model spectrum by an instrumental broadening of $R = 2165$, as expected for the R2000B grating. We then scaled the model to observational fluxes by multiplying by the solid angle, Ω . We then applied the input interstellar reddening to the model, and finally applied rotational broadening with a kernel determined from the Claret 4-term limb darkening law evaluated in the SDSS g -band.

We calculated synthetic photometry in each of the observed bands, by integrating the model over each bandpass, to compare against the observed fluxes, where we assumed each flux contained an additional 0.01 mag systematic uncertainty. To compare with the spectral data, we normalised the model against the spectrum using a spline fit to their spectral ratio (in order to remove the effects of imperfect flux calibration). We determined the total χ^2 fit by adding the individual χ^2 for the spectrum and photometry. We also included the measured reddening $E(B-V) = 0.27 \pm 0.05$ from the 3D extinction maps of Lallement

et al. (2014) as an additional data-point in the total χ^2 effectively acting as a prior on our fitted reddening parameter.

After performing this minimization, we found $T_{\text{eff}} = 27,330 \pm 370$ K, $\log g = 6.213 \pm 0.050$ dex (cm s^{-2}), $\log(\text{He}/\text{H}) = -2.20 \pm 0.03$ dex, $\Omega = (9.41 \pm 0.23) \times 10^{-24}$ sr, $E(B-V) = 0.383 \pm 0.007$, and $v_{\text{eq}} \sin i = 299 \pm 10$ km s^{-1} . All quoted uncertainties are determined from the covariance matrix of the best fit. From these we determined the stellar radius to be $R_{\text{ELM}} = 0.065 \pm 0.005 R_{\odot}$, the ELM white dwarf mass to be $M_{\text{ELM}} = 0.257 \pm 0.049 M_{\odot}$, and their Pearson correlation as $\rho = 0.785$. From the best fitting model spectrum, we determined the intrinsic *Gaia* absolute magnitude to be $G_{\text{abs}} = 6.73 \pm 0.17$ mag (with the uncertainty considering the errors on Ω and the parallax) and its *Gaia* colour to be $Bp - Rp = -0.419 \pm 0.005$.

An important source of uncertainty in our fit is the degree of rotational broadening. Our radius and orbital period measurements (assuming tidal locking) suggest $v_{\text{eq}} = 231 \pm 17$ km s^{-1} , which is notably smaller than our measured value of $v_{\text{eq}} \sin i$ (our light curve analysis in the following section indicates an inclination of 65 ± 7 degrees). While we cannot provide a definite explanation for this discrepancy, we acknowledge that our model of rotational broadening does not account for ellipsoidal distortion of the star or gravity darkening which will certainly lead to more complex broadening. Nevertheless, we do not believe this invalidates our other stellar parameters, as our measured $v_{\text{eq}} \sin i$ simply represents the best fitting value with an incomplete model. If we adopt an alternative broadening profile such a rectangular distribution (which gives more weight to the most extreme Doppler shifts), we find a lower value of $v_{\text{eq}} \sin i = 247 \pm 10$ km s^{-1} , while the other parameters are virtually unchanged.

4.3. Light curve fit

The ULTRASPEC light curve shows sinusoidal variations on half the orbital period, indicating that we are seeing ellipsoidal modulation originating from the tidally distorted ELM white dwarf. We can use the amplitude of this variation to set constraints on the stellar and binary parameters since the fractional semi-amplitude is given by

$$\frac{\partial F}{F} = 0.15 \frac{(15 + u_1)(1 + \beta_1)}{3 - u_1} \left(\frac{R_1}{a}\right)^3 q \sin^2 i, \quad (1)$$

(Morris & Naftilan 1993; Zucker et al. 2007) where u_1 is the linear limb-darkening coefficient, β_1 is the gravity darkening exponent, R_1/a is the radius scaled by the orbital separation, $q = M_2/M_1$ is the mass ratio and i is the inclination. The subscript 1 refers to the ELM white dwarf, while 2 refers to the white dwarf companion.

In the absence of any additional information when fitting the ellipsoidal modulation there is complete degeneracy between the mass ratio, scaled radius of the ELM white dwarf and inclination. Therefore, we use the constraints on the mass and radius of the ELM white dwarf (i.e. M_1 and R_1) from the spectral modelling to break some of this degeneracy, resulting in the ellipsoidal amplitude depending only on M_2 and i (since a is a function of M_1 , M_2 and P_{orb}), essentially allowing us to place constraints on the mass of the unseen white dwarf companion from the light curve.

Rather than simply using Equation 1 (which ignores any contribution from the companion or any irradiation effects and does not allow a more sophisticated treatment of limb darkening), we modelled the light curve in a more complete way using *LCURVE*

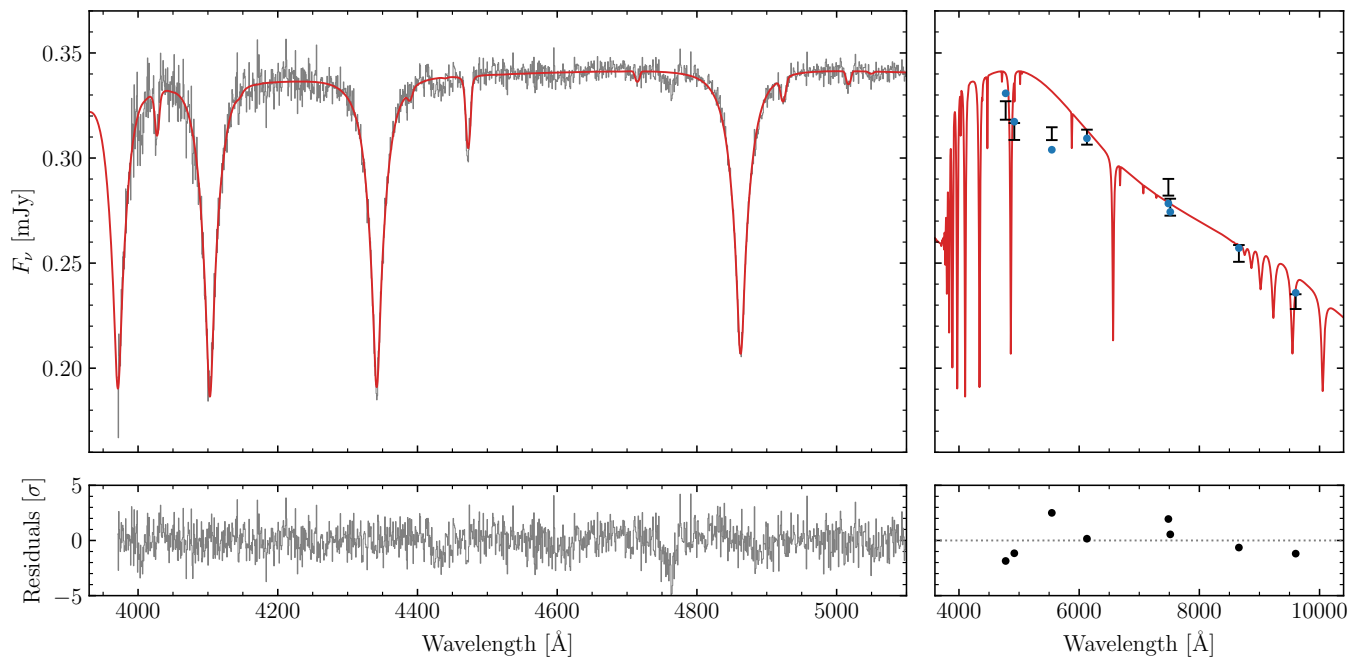


Fig. 4. Fit to the spectrum of J0526+5934 (left panels) with the residuals shown below. The best fitting model (red) includes the measured interstellar reddening. The spectral fluxes have been re-calibrated against the model with a spline fit to their ratio. While the GTC spectrum extends to 5700 Å, it is featureless beyond 5100 Å, and so those wavelengths are not shown. The same model is shown against the photometry (black error bars), with synthetic photometry shown by the blue points (right panels). Error bars include the assumed 0.01 mag systematic uncertainty. Again, their residuals are shown below.

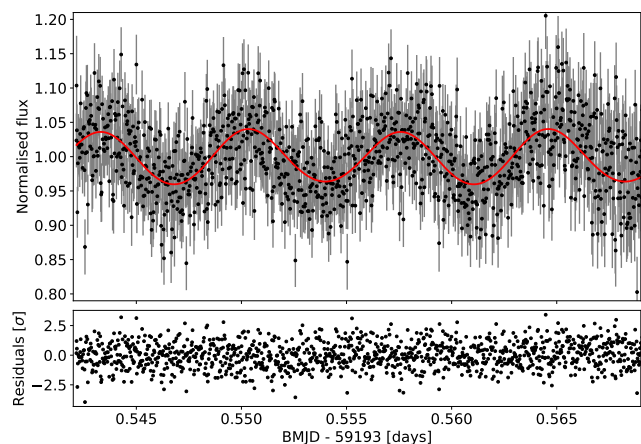


Fig. 5. ULTRASPEC *KG5* band light curve with best fit model overplotted in red. The bottom panel shows the residuals to this fit in terms of standard deviations from the model.

(Copperwheat et al. 2010) and fitted the ULTRASPEC data using the Markov chain Monte Carlo (MCMC) method (Press et al. 2007), implemented using the Python package `EMCEE` (Foreman-Mackey et al. 2013). The fitted parameters were: the mass of the ELM white dwarf (M_1), the mass of the white dwarf companion (M_2), the radius of the ELM white dwarf (R_1), the inclination (i), the time of the superior conjunction of the ELM white dwarf (T_0) and the orbital period (P_{orb}). No limb-darkening coefficients or gravity darkening exponents have been computed for the parameter space of the ELM white dwarf in the ULTRASPEC *KG5* filter. Therefore, following the method in Claret et al. (2020), we created a small grid of limb-darkening (4-term law) and gravity darkening values in the *KG5* band for a white dwarf effective

temperature of 27,000 K and a range of surface gravities between 6.0 and 6.5 in steps of 0.1 dex, using updated model DA spectra from Koester (2010)². Then for a chosen value of M_1 and R_1 we computed the limb-darkening coefficient and gravity darkening exponent of the ELM white dwarf by interpolating this grid. We fixed the temperature of the ELM white dwarf to the spectroscopically determined value of 27,330 K and also fixed the temperature of the white dwarf companion. Given that the companion contributes a negligible amount of flux to the ULTRASPEC light curve the choice of temperature is somewhat arbitrary. Nevertheless, to check that this parameter has no effect on the final results we fitted the light curve twice, once with the temperature of the companion fixed at 8,000 K and again with it fixed at 20,000 K. We also fixed the radius of the companion to a typical white dwarf radius of $0.015 R_{\odot}$. Again, this parameter makes little difference given the extreme flux ratio in the *KG5* band.

We placed a multivariate Gaussian prior on M_1 and R_1 with a correlation value of $\rho_{MR} = 0.785$, based on the spectroscopically derived values, which takes into account the fact that these two parameters are strongly correlated. We placed a Gaussian prior on P_{orb} based on the TJO and GTC results and a uniform prior on the inclination between 1 and 90 degrees. We also used the radial velocity curve to determine which minimum in the light curve corresponded to the superior conjunction of the ELM white dwarf and placed a uniform prior on T_0 between the time

² Note that the dominant source of continuum opacity in the visible component of J0526+5934 is from hydrogen. The additional continuum opacity from the $\approx 1\%$ of He in the atmosphere is negligible. Indeed, limb- and gravity-darkening coefficients derived from a pure-hydrogen DA model (i.e. without He traces) of the same effective temperature and surface gravity as our best-fit model are nearly identical to those directly obtained from the best-fit model.

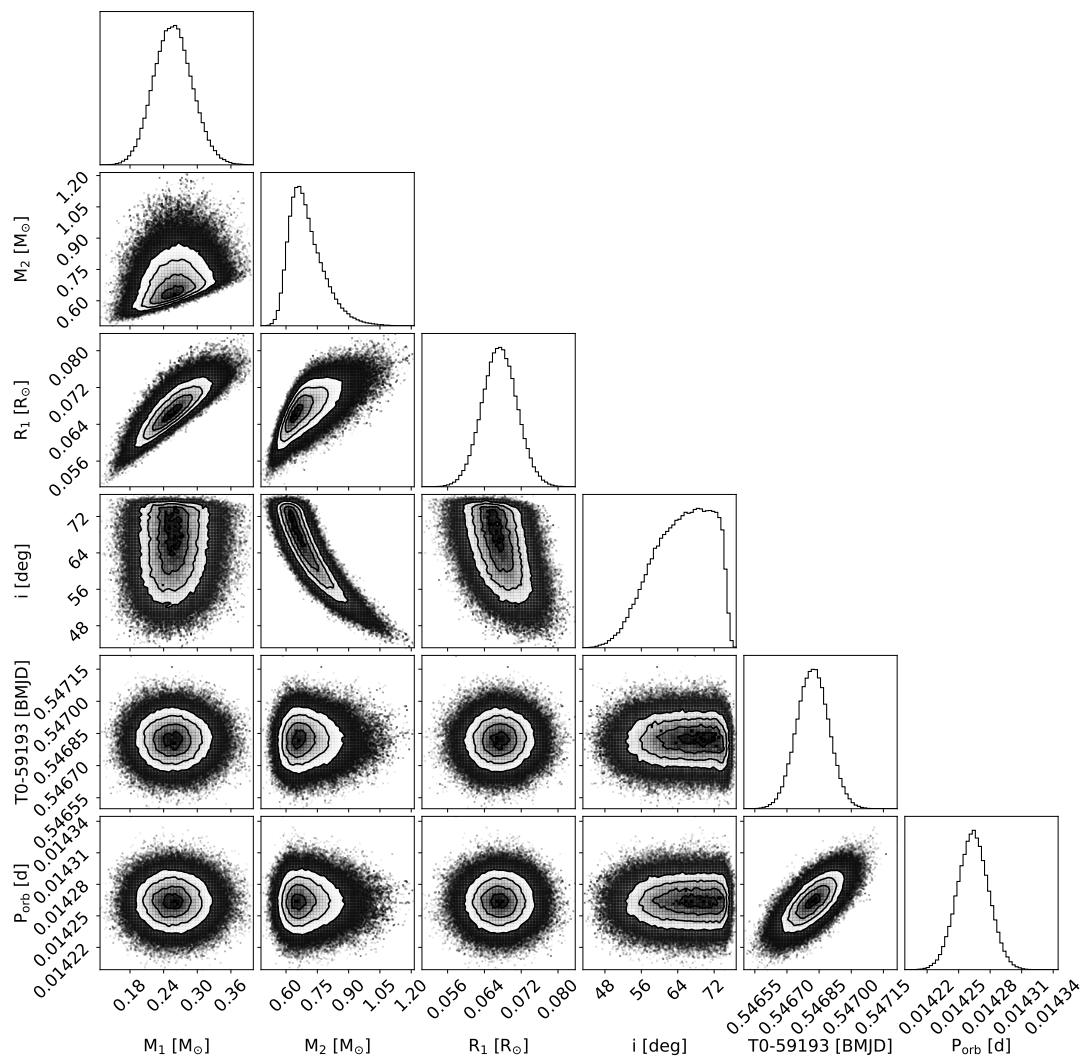


Fig. 6. Posterior probability distributions for model parameters obtained through fitting the ULTRASPEC *KG5* band light curve. Grey-scales and contours represent the joint probability distributions for each pair of parameters, while the histograms show the marginalised probability distributions for each parameter.

of this minimum and $\pm 0.5 P_{\text{orb}}$ to ensure that the fit did not try to jump to the next cycle. Finally, at each step in the fitting process we computed the radial velocity semi-amplitude of the ELM white dwarf (which is only a function of M_1 , M_2 , P_{orb} and i) and compared this to the measured value via a Gaussian prior based on the measured value. This final constraint helps break some of the degeneracy between M_2 and i .

Our MCMC fitting used 50 walkers, each with 20,000 points. The first 5,000 points were classed as "burn-in" and were removed from the final results. The ULTRASPEC light curve and best fit model is shown in Figure 5, while the posterior probability distributions are shown in Figure 6. As expected we found no difference in the results between an 8,000 K and 20,000 K companion. We found that inclinations greater than around 75 degrees are excluded, since we would expect to see the ELM white dwarf eclipsed by its companion at these high inclinations (which is not seen in the light curve). Inclinations lower than around 40 degrees are also ruled out, since at these low inclinations it is not possible to generate a large enough ellipsoidal signal in the light curve while simultaneously being consistent with the measured radial velocity semi-amplitude of the ELM white dwarf. The best consistency is found at higher inclina-

tions, hence lower companion white dwarf masses, as reflected in the marginalised probability distribution for M_2 in Figure 6. Overall we constrain the inclination to 65 ± 7 degrees and the companion white dwarf mass to $0.71^{+0.09}_{-0.06} M_{\odot}$. This mass is consistent with our assumption that the unseen companion is a white dwarf. The distributions for P_{orb} , M_1 and R_1 are entirely driven by the priors placed on these values, while we find a value for T_0 of BMJD(TDB) = 59193.54682(7), where the number in the parenthesis represents the uncertainty on the final digit.

4.4. Effective temperature of the white dwarf companion

We attempted to obtain an upper limit to the white dwarf companion's effective temperature by determining by how much the synthetic spectrum of a (hydrogen-rich) white dwarf can be added to the spectrum of the ELM white dwarf without affecting the observed spectral features. To that end we considered the best-fit model to the observed GTC combined spectrum from Section 4.2 and subtracted model spectra from the Koester (2010) updated collection of any given effective temperature and surface gravity between 7.8 and 8.3 dex (that is a surface gravity that corresponds to a mass of $0.71^{+0.09}_{-0.06} M_{\odot}$, as derived from the

Table 1. Orbital and stellar parameters for the visible component and the unseen companion of J0526+5934. We include the values measured by Kosakowski et al. (2023b) and Lin et al. (2023) for comparison.

Binary	This work	Kosakowski et al. (2023b)	Lin et al. (2023)
Orbital period (s)	1232.00 ± 0.66	1230.37467 ± 0.00007	1230.374556 ± 0.000318
Orbital inclination (°)	65 ± 7	57.1 ^{+4.3} _{-4.1}	68.2 ^{+3.7} _{-5.2}
Systemic velocity (km/s)	-21.6 ± 2.2	-40.7 ± 4.1	-35.6 ± 4.4
Visible component			
T _{eff} (K)	27,330 ± 370	27,300 ± 260	25,480 ± 360
log g (dex)	6.213 ± 0.050	6.37 ± 0.03	6.355 ± 0.068
M (M _⊙)	0.257 ± 0.049	0.378 ^{+0.066} _{-0.060}	0.360 ^{+0.080} _{-0.071}
R (R _⊙)	0.065 ± 0.005	0.070 ± 0.005	0.0661 ± 0.0054
[He/H] (dex)	-2.20 ± 0.03	-2.45 ± 0.06	-2.305 ± 0.062
K (km/s)	565.2 ± 3.2	558.3 ± 4.8	559.6 ^{+6.4} _{-6.5}
Unseen WD			
M (M _⊙)	0.71 ^{+0.09} _{-0.06}	0.887 ^{+0.110} _{-0.098}	0.735 ^{+0.075} _{-0.069}
T _{eff} (K)	<6700	-	-

light curve fit). After subtracting each white dwarf model, we measured the resulting H β equivalent width (EW). We assumed the spectral features to be different from those sampled by the best-fit model to the observed spectrum when the EW decreased by more than 25%. Fitting such spectra would result in stellar parameters that would be different to those obtained in Section 4.2 due to the change in the Balmer line profiles. However, we found that the EW remain unaltered in all cases, with the ELM contribution to the total flux being always larger than 96%. This implied no constraint on the unseen white dwarf companion's effective temperature could be placed with this exercise. More stringent constraints on this value are discussed in Section 5.

4.5. Comparison to Kosakowski et al. (2023b) and Lin et al. (2023)

The most relevant orbital and stellar parameters we have obtained throughout this section for J0526+5934 are provided in Table 1. All our measured values are similar to those recently obtained by Kosakowski et al. (2023b) and Lin et al. (2023), although slight differences arise (see Table 1). The most important difference in the context of this paper is that we derive a lower surface gravity for the visible component and, as a consequence, a lower mass. In the three studies, these values are directly obtained from the spectral fitting analysis. Whilst our observational strategy ensured we are not suffering from orbital smearing (Section 4.1), the exposure times used during the spectroscopic observations performed by Kosakowski et al. (2023b) covered $\approx 10\%$ of the orbit, therefore their combined spectrum was considerably affected by smearing. The observations carried out by Lin et al. (2023) were clearly affected by this effect too. Although the authors fitted all their spectra simultaneously to account for this, our results should yield more accurate values simply because orbital smearing is efficiently taken into account. As a consequence, our derived mass provides robust evidence for the visible component in J0526+5934 not to necessarily be a hot subdwarf star, but rather an ELM white dwarf, as we have been assuming in this paper. In the following section we discuss this hypothesis in detail.

5. Discussion

The deduced stellar mass values for the bright component of J0526+5934 strongly reduce the likelihood of it being a hot sub-

dwarf star. In fact, the minimum mass requirement for a subdwarf star typically stands at approximately $0.30 M_{\odot}$ (Arancibia-Rojas et al. 2024). In particular, detailed calculations by Han et al. (2003) predict this minimum mass to be about $0.33 M_{\odot}$. This is due to the fact that stars below this mass threshold are unable to initiate core-helium burning within their cores under nondegenerate conditions. From the observational point of view, the mass distribution of hot subdwarf stars has been found to range between $\approx 0.3 M_{\odot}$ and $0.63 M_{\odot}$, with a clear peak at $\approx 0.45 M_{\odot}$ and very few objects below $\approx 0.3 M_{\odot}$ (Fontaine et al. 2012; Schaffenroth et al. 2022; Lei et al. 2023). This gives further support to our hypothesis that the visible component of J0526+5934 is an ELM white dwarf.

ELM white dwarfs are expected to originate from unstable mass loss through the common envelope ejection channel and the stable Roche lobe overflow channel, as discussed recently by Li et al. (2019). Existing evolutionary tracks for ELM white dwarfs are based on the assumption of stable Roche lobe overflow, involving stable mass transfer (see Althaus et al. 2013; Istrate et al. 2016 and references therein). Consequently, ELM white dwarf evolutionary models derived under this framework are characterized by an upper limit on the possible H-layer thickness that a given-mass ELM white dwarf model can possess. This implies that residual stable hydrogen burning emerges as the primary energy source during the cooling phase of the white dwarf, leading to the occurrence of multiple hydrogen flashes at the onset of the cooling track.

The manifestation of hydrogen flashes results in diverse potential solutions for the observed ELM white dwarf component. Specifically, from the evolutionary sequences computed by Althaus et al. (2013), we deduced a stellar mass of $0.237 \pm 0.035 M_{\odot}$, a radius of $0.06 \pm 0.006 R_{\odot}$, a cooling age of 260 ± 240 Myr, and a helium surface abundance [He/H] in the range of -2. and -4. These values perfectly agree with the observational inferences for the J0526+5934 bright component (Section 4.2), thus giving strong support for the visible object to be an ELM white dwarf. In particular, the derived mass value is in agreement with the predictions of population property studies of ELM white dwarfs in double degenerate systems, which suggests that intrinsic masses for ELM white dwarfs peak around $0.25 M_{\odot}$ for the CE channel (Li et al. 2019). The considerable range in derived cooling ages are the result of residual hydrogen burning in the envelope.

It is noteworthy that the helium abundance predicted by cooling sequences is also in agreement with our independent value

obtained from the spectral analysis performed in Section 4.2. Gravitational settling rapidly depletes metals in the atmospheres of white dwarfs; however, due to the lower surface gravities characterizing ELM white dwarfs, the impact of gravitational settling is less pronounced. This explains that traces of helium persist in the envelope at the effective temperature of the ELM component. For low-mass ELM white dwarfs, a pure hydrogen envelope is expected, albeit at significantly lower effective temperatures. The helium abundances predicted by the cooling sequences of Althaus et al. (2013) are likely a conservative lower limit. Higher helium abundances could potentially be expected due to rotational mixing, countering the effects of gravitational settling in the surface layers of young ELM proto-white dwarfs. However, as the ELM contracts and embarks on its cooling track, the efficiency of rotational mixing diminishes, and the role of rotation in augmenting helium abundance becomes less significant, as discussed by Istrate et al. (2016).

The formation of ELM white dwarfs with hydrogen contents lower than expected from stable Roche lobe overflow cannot be ruled out. Specifically, Strickler et al. (2009) concluded that the presence of a population of low-mass He-core white dwarfs with thin hydrogen envelopes in NGC 6397 cannot be discarded. More recently, Irrgang et al. (2021) demonstrated the necessity of a thin H envelope in J1604+1000, a proto-ELM white dwarf weighing approximately $0.21 M_{\odot}$ likely resulting from a common envelope event. Moreover, a comparative analysis of the mass distribution of observed ELM white dwarfs with theoretical expectations by Li et al. (2019) has suggested that the ELM white dwarfs arising from the common envelope channel could be characterized by thinner H envelope compared to those resulting from stable Roche lobe channel. Finally, asteroseismological analysis support the presence of thin H envelopes (1-2 order of magnitude thinner than predicted by the stable Roche lobe overflow channel) in certain pulsating ELM white dwarfs (Calcaferro et al. 2018b).

While the majority of ELM white dwarfs are discovered in double white dwarf systems resulting from common envelope episodes, nearly all evolutionary calculations that involve stable mass transfer are applied to derive the properties of the white dwarf components in such systems. However, it could be expected that in ELM white dwarfs resulting from common envelope, the recurrent hydrogen shell flashes may not occur, because of the minor role of residual H burning. In fact, the evolution of proto-ELM white dwarfs depends on the mass of the hydrogen-rich layer above the helium core, which is determined by the detailed common envelope ejection process, the most uncertain phase in binary evolution (Li et al. 2019). A reduction in the thickness of the hydrogen envelope by a factor of 2 causes residual hydrogen burning to become negligible (Calcaferro et al. 2018a). With these considerations in mind, i.e. neglecting the occurrence of hydrogen flashes, we should expect a stellar mass of approximately $0.27 M_{\odot}$, also in agreement with the observational inference. The resulting cooling times are expected to be much shorter than the cooling times of their counterpart with thick hydrogen envelope (see Calcaferro et al. 2018a).

From the observational data of J0526+5934 and based on the probable initial configuration of the system and cooling times, we can infer an upper limit on the effective temperature of the unseen white dwarf companion. According to Li et al. (2019), the most likely progenitors of ELM white dwarfs from common envelope channel have masses in the range 0.95 - $1.25 M_{\odot}$. Given that the common envelope channel is responsible for ELM white dwarfs in double degenerate systems with a helium-core white dwarf more massive than about $0.22 M_{\odot}$ (Li et al. 2019), we

adopt a value of $1.25 M_{\odot}$ as the maximum stellar mass for the progenitor of the ELM component. This would yield an age of approximately 3.8 Gyr for the progenitor to leave the main sequence (Miller Bertolami 2016). Considering the potential mass range for the unseen white dwarf companion (Table 1), the minimum mass of its progenitor would be on the order of $3.0 M_{\odot}$, suggesting a main sequence lifetime of 0.3 Gyr (Miller Bertolami 2016). Thus, the newly formed white dwarf should have been undergoing cooling for at least 3.5 Gyr. During this period, and depending on its mass, the invisible white dwarf component should have attained an effective temperature within the range of 5700-6700K. These inferred values serve as upper limits considering that the ELM could have arisen from a progenitor less massive than $1.25 M_{\odot}$.

By considering J0526+5934 as a compact binary star composed of two white dwarfs of masses of $0.26 M_{\odot}$ and $0.71 M_{\odot}$ (Table 1), we estimate the merger time due to the emission of gravitational waves (τ ; in Myr) from the following expression:

$$\tau = 47925 \frac{(M_1 + M_2)^{1/3}}{M_1 M_2} P^{8/3}, \quad (2)$$

where P is the orbital period in days and the masses are in units of M_{\odot} (Kraft et al. 1962). This results in just ≈ 3 Myr. The result of the merger, assuming no mass loss takes place during the process, would be a massive ($\approx 1 M_{\odot}$) white dwarf. A relatively large percentage of such massive white dwarfs is expected to arise from this kind of mergers (Cheng et al. 2019; Temmink et al. 2020; Kilic et al. 2023), which can partially explain the high-mass excess observed in the white dwarf mass distributions over the last years (Rebassa-Mansergas et al. 2015a,b; Jiménez-Esteban et al. 2023; Kilic et al. 2020). It is also possible that the system ends up as a .Ia supernovae. As indicated by Shen (2015), in this scenario the ELM white dwarf would begin transferring material (sufficiently enriched in He) and a He detonation would occur during the subsequent merger of the two white dwarfs, thus producing a .Ia supernovae.

6. Summary and conclusions

We have presented an independent observational and theoretical study of the ultra-short period binary J0526+5934. The observations were carried out at the Telescopi Joan Oró, The Gran Telescopio Canarias and the Thai National Telescope, and the evolutionary models employed were those from the La Plata group. We have provided constraints on the orbital and stellar parameters of both stellar components. Our results are similar to those obtained by the previous analysis of Kosakowski et al. (2023b) and Lin et al. (2023). However, we find a mass for the visible component of $0.26 \pm 0.05 M_{\odot}$ (from the observational analysis) or $0.237 \pm 0.035 M_{\odot}$ (from the theoretical evolutionary tracks). This is lower than the reported values of $0.378^{+0.066}_{-0.060} M_{\odot}$ by Kosakowski et al. (2023b) and $0.360^{+0.080}_{-0.071} M_{\odot}$ by Lin et al. (2023). This difference is key when interpreting the nature of the visible component. Whilst the results of Kosakowski et al. (2023b) and Lin et al. (2023) favour a hot subdwarf star, our analysis is much more in agreement with an extremely low-mass white dwarf. The three studies cannot completely rule out the alternative scenario and future observations may shed further insight on this remarkable object.

Acknowledgements. This work was partially supported by the Spanish MINECO grant PID2020-117252GB-I00 and by the AGAUR/Generalitat de Catalunya grant SGR-386/2021. SGP acknowledges the support of a Science and

Technology Facilities Council (STFC) Ernest Rutherford Fellowship. IP acknowledges support from a Royal Society University Research Fellowship (URF\R1\231496). RR acknowledges support from Grant RYC2021-030837-I funded by MCIN/AEI/ 10.13039/501100011033 and by “European Union NextGeneration EU/PRTR”. M.C. acknowledges grant RYC2021-032721-I, funded by MCIN/AEI/10.13039/501100011033 and by the European Union46 NextGenerationEU/PRTR. This research made use of data from the European Space Agency (ESA) mission *Gaia* (<https://www.cosmos.esa.int/gaia>), processed by the *Gaia* Data Processing and Analysis Consortium (DPAC, <https://www.cosmos.esa.int/web/gaia/dpac/consortium>). Funding for the DPAC has been provided by national institutions, in particular the institutions participating in the *Gaia* Multilateral Agreement. This work makes use of data from the 80 cm Telescopi Joan Oró (TJO) of the Montsec Astronomical Observatory (OAdM), owned by the Generalitat de Catalunya and operated by the Institut d’Estudis Espacials de Catalunya (IEEC). Based on observations obtained with the Samuel Oschin Telescope 48 inch and the 60 inch telescope at the Palomar Observatory as part of the Zwicky Transient Facility project. Based on observations made with the Gran Telescopio Canarias (programme GTC6-21B), installed in the Spanish Observatorio del Roque de los Muchachos of the Instituto de Astrofísica de Canarias, in the island of La Palma.

References

- Althaus, L. G., Córscico, A. H., Isern, J., & García-Berro, E. 2010, *A&A Rev.*, 18, 471
- Althaus, L. G., Miller Bertolami, M. M., & Córscico, A. H. 2013, *A&A*, 557, A19
- Arancibia-Rojas, E., Zorotovic, M., Vučković, M., et al. 2024, *MNRAS*, 527, 11184
- Bauer, E. B., Schwab, J., Bildsten, L., & Cheng, S. 2020, *ApJ*, 902, 93
- Bell, K. J., Gianninas, A., Hermes, J. J., et al. 2017, *ApJ*, 835, 180
- Blouin, S., Dufour, P., Thibeault, C., & Allard, N. F. 2019, *ApJ*, 878, 63
- Breedt, E., Steeghs, D., Marsh, T. R., et al. 2017, *MNRAS*, 468, 2910
- Brown, W. R., Gianninas, A., Kilic, M., Kenyon, S. J., & Allende Prieto, C. 2016, *ApJ*, 818, 155
- Brown, W. R., Kilic, M., Hermes, J. J., et al. 2011, *ApJ*, 737, L23
- Brown, W. R., Kilic, M., Kosakowski, A., et al. 2020, *ApJ*, 889, 49
- Brown, W. R., Kilic, M., Kosakowski, A., & Gianninas, A. 2022, *ApJ*, 933, 94
- Burdge, K. B., Coughlin, M. W., Fuller, J., et al. 2020, *ApJ*, 905, L7
- Burdge, K. B., Coughlin, M. W., Fuller, J., et al. 2019a, *Nature*, 571, 528
- Burdge, K. B., Fuller, J., Phinney, E. S., et al. 2019b, *ApJ*, 886, L12
- Calcaferro, L. M., Althaus, L. G., & Córscico, A. H. 2018a, *A&A*, 614, A49
- Calcaferro, L. M., Córscico, A. H., Althaus, L. G., Romero, A. D., & Kepler, S. O. 2018b, *A&A*, 620, A196
- Camacho, J., Torres, S., García-Berro, E., et al. 2014, *A&A*, 566, A86
- Camisassa, M., Torres, S., Hollands, M., et al. 2023, *A&A*, 674, A213
- Camisassa, M. E., Althaus, L. G., Córscico, A. H., et al. 2019, *A&A*, 625, A87
- Camisassa, M. E., Althaus, L. G., Córscico, A. H., et al. 2016, *ApJ*, 823, 158
- Cheng, S., Cummings, J. D., & Ménard, B. 2019, *ApJ*, 886, 100
- Claret, A., Cukanovaite, E., Burdge, K., et al. 2020, *A&A*, 634, A93
- Cojocaru, R., Rebassa-Mansergas, A., Torres, S., & García-Berro, E. 2017, *MNRAS*, 470, 1442
- Copperwheat, C. M., Marsh, T. R., Dhillon, V. S., et al. 2010, *MNRAS*, 402, 1824
- Dekany, R., Smith, R. M., Riddle, R., et al. 2020, *PASP*, 132, 038001
- Dhillon, V. S., Marsh, T. R., Atkinson, D. C., et al. 2014, *MNRAS*, 444, 4009
- Dhillon, V. S., Marsh, T. R., Stevenson, M. J., et al. 2007, *MNRAS*, 378, 825
- Fontaine, G., Brassard, P., Charpinet, S., et al. 2012, *A&A*, 539, A12
- Foreman-Mackey, D., Hogg, D. W., Lang, D., & Goodman, J. 2013, *PASP*, 125, 306
- Gaia* Collaboration, Brown, A. G. A., Vallenari, A., et al. 2018, *A&A*, 616, A1
- Gaidos, E., Claytor, Z., Dungee, R., Ali, A., & Feiden, G. A. 2023, *MNRAS*, 520, 5283
- García-Berro, E., Hernanz, M., Isern, J., & Mochkovitch, R. 1988, *Nature*, 333, 642
- García-Berro, E., Torres, S., Althaus, L. G., et al. 2010, *Nature*, 465, 194
- Ge, H., Webbink, R. F., Chen, X., & Han, Z. 2015, *ApJ*, 812, 40
- Geier, S. 2020, *A&A*, 635, A193
- Gianninas, A., Kilic, M., Brown, W. R., Canton, P., & Kenyon, S. J. 2015, *ApJ*, 812, 167
- Hallakoun, N., Maoz, D., Kilic, M., et al. 2016, *MNRAS*, 458, 845
- Han, Z., Podsiadlowski, P., Maxted, P. F. L., & Marsh, T. R. 2003, *MNRAS*, 341, 669
- Hardy, L. K., McAllister, M. J., Dhillon, V. S., et al. 2017, *MNRAS*, 465, 4968
- Hollands, M. A., Tremblay, P. E., Gänsicke, B. T., Gentile-Fusillo, N. P., & Toonen, S. 2018, *MNRAS*, 480, 3942
- Iben, I., J. & Tutukov, A. V. 1984, *ApJS*, 54, 335
- Inight, K., Gänsicke, B. T., Breedt, E., et al. 2021, *MNRAS*, 504, 2420
- Irrgang, A., Geier, S., Heber, U., et al. 2021, *A&A*, 650, A102
- Istrate, A. G., Marchant, P., Tauris, T. M., et al. 2016, *A&A*, 595, A35
- Jeffery, E. J., von Hippel, T., DeGennaro, S., et al. 2011, *ApJ*, 730, 35
- Jiménez-Esteban, F. M., Torres, S., Rebassa-Mansergas, A., et al. 2023, *MNRAS*, 518, 5106
- Keller, P. M., Breedt, E., Hodgkin, S., et al. 2022, *MNRAS*, 509, 4171
- Kilic, M., Bergeron, P., Kosakowski, A., et al. 2020, *ApJ*, 898, 84
- Kilic, M., Brown, W. R., Gianninas, A., et al. 2017, *MNRAS*, 471, 4218
- Kilic, M., Moss, A. G., Kosakowski, A., et al. 2023, *MNRAS*, 518, 2341
- Koester, D. 2010, *Mem. Soc. Astron. Italiana*, 81, 921
- Korol, V., Koop, O., & Rossi, E. M. 2018, *ApJ*, 866, L20
- Kosakowski, A., Brown, W. R., Kilic, M., et al. 2023a, *ApJ*, 950, 141
- Kosakowski, A., Kilic, M., Brown, W. R., Bergeron, P., & Kupfer, T. 2022, *MNRAS*, 516, 720
- Kosakowski, A., Kupfer, T., Bergeron, P., & Littenberg, T. B. 2023b, *ApJ*, 959, 114
- Kraft, R. P., Mathews, J., & Greenstein, J. L. 1962, *ApJ*, 136, 312
- Lallement, R., Vergely, J. L., Valette, B., et al. 2014, *A&A*, 561, A91
- Lei, Z., He, R., Németh, P., et al. 2023, *ApJ*, 953, 122
- Li, Z., Chen, X., Chen, H.-L., & Han, Z. 2019, *ApJ*, 871, 148
- Lin, J., Wu, C., Xiong, H., et al. 2023, arXiv e-prints, arXiv:2312.13612
- Liu, D., Wang, B., & Han, Z. 2018, *MNRAS*, 473, 5352
- Maoz, D., Hallakoun, N., & Badenes, C. 2018, *MNRAS*, 476, 2584
- Marsh, T. R. 1989, *PASP*, 101, 1032
- Masci, F. J., Laher, R. R., Rusholme, B., et al. 2019, *PASP*, 131, 018003
- McCleery, J., Tremblay, P.-E., Gentile Fusillo, N. P., et al. 2020, *MNRAS*, 499, 1890
- Miller Bertolami, M. M. 2016, *A&A*, 588, A25
- Morgan, D. P., West, A. A., Garcés, A., et al. 2012, *AJ*, 144, 93
- Morris, S. L. & Naftilan, S. A. 1993, *ApJ*, 419, 344
- Munday, J., Tremblay, P. E., Hermes, J. J., et al. 2023, *MNRAS*, 525, 1814
- Napiwotzki, R., Karl, C. A., Lisker, T., et al. 2020, *A&A*, 638, A131
- Nelemans, G. & Tout, C. A. 2005, *MNRAS*, 356, 753
- O’Brien, M. W., Tremblay, P. E., Klein, B. L., et al. 2024, *MNRAS*, 527, 8687
- Oswalt, T. D., Smith, J. A., Wood, M. A., & Hintzen, P. 1996, *Nature*, 382, 692
- Parsons, S. G., Brown, A. J., Littlefair, S. P., et al. 2020, *Nature Astronomy*, 4, 690
- Parsons, S. G., Gänsicke, B. T., Marsh, T. R., et al. 2017, *MNRAS*, 470, 4473
- Parsons, S. G., Gänsicke, B. T., Marsh, T. R., et al. 2018, *MNRAS*, 481, 1083
- Pelisolì, I., Kepler, S. O., Koester, D., et al. 2018, *MNRAS*, 478, 867
- Pelisolì, I. & Vos, J. 2019, *MNRAS*, 488, 2892
- Press, W. H., Teukolsky, A. A., Vetterling, W. T., & Flannery, B. P. 2007, *Numerical recipes. The art of scientific computing*, 3rd edn. (Cambridge: University Press)
- Raddi, R., Torres, S., Rebassa-Mansergas, A., et al. 2022, *A&A*, 658, A22
- Rebassa-Mansergas, A., Anguiano, B., García-Berro, E., et al. 2016, *MNRAS*, 463, 1137
- Rebassa-Mansergas, A., Liu, X. W., Cojocaru, R., et al. 2015a, *MNRAS*, 450, 743
- Rebassa-Mansergas, A., Maldonado, J., Raddi, R., et al. 2021, *MNRAS*, 505, 3165
- Rebassa-Mansergas, A., Maldonado, J., Raddi, R., et al. 2023, *MNRAS*, 526, 4787
- Rebassa-Mansergas, A., Parsons, S. G., Dhillon, V. S., et al. 2019a, *Nature Astronomy*, 3, 553
- Rebassa-Mansergas, A., Parsons, S. G., García-Berro, E., et al. 2017, *MNRAS*, 466, 1575
- Rebassa-Mansergas, A., Rybicka, M., Liu, X. W., Han, Z., & García-Berro, E. 2015b, *MNRAS*, 452, 1637
- Rebassa-Mansergas, A., Schreiber, M. R., & Gänsicke, B. T. 2013, *MNRAS*, 429, 3570
- Rebassa-Mansergas, A., Toonen, S., Korol, V., & Torres, S. 2019b, *MNRAS*, 482, 3656
- Ren, L., Li, C., Ma, B., et al. 2023, *ApJS*, 264, 39
- Schaffneroth, V., Pelisolì, I., Barlow, B. N., Geier, S., & Kupfer, T. 2022, *A&A*, 666, A182
- Schreiber, M. R., Belloni, D., Zorotovic, M., et al. 2022, *MNRAS*, 513, 3090
- Schreiber, M. R., Gänsicke, B. T., Rebassa-Mansergas, A., et al. 2010, *A&A*, 513, L7
- Shen, K. J. 2015, *ApJ*, 805, L6
- Skinner, J. N., Morgan, D. P., West, A. A., Lépine, S., & Thorstensen, J. R. 2017, *AJ*, 154, 118
- Strickler, R. R., Cool, A. M., Anderson, J., et al. 2009, *ApJ*, 699, 40
- Temminck, K. D., Toonen, S., Zapartas, E., Justham, S., & Gänsicke, B. T. 2020, *A&A*, 636, A31
- Torres, S., García-Berro, E., Althaus, L. G., & Camisassa, M. E. 2015, *A&A*, 581, A90
- Torres, S., Rebassa-Mansergas, A., Camisassa, M. E., & Raddi, R. 2021, *MNRAS*, 502, 1753
- van der Sluys, M. V., Verbunt, F., & Pols, O. R. 2006, *A&A*, 460, 209
- van Roestel, J., Kupfer, T., Bell, K. J., et al. 2021, *ApJ*, 919, L26
- Wang, K., Németh, P., Luo, Y., et al. 2022, *ApJ*, 936, 5
- Webbink, R. F. 2008, in *Astrophysics and Space Science Library*, Vol. 352, Astrophysics and Space Science Library, ed. E. F. Milone, D. A. Leahy, & D. W. Hobill, 233
- Whelan, J. & Iben, I. 1973, *ApJ*, 186, 1007
- Woods, T. E., Ivanova, N., van der Sluys, M. V., & Chaichenet, S. 2012, *ApJ*, 744, 12
- Zorotovic, M. & Schreiber, M. 2022, *MNRAS*, 513, 3587
- Zorotovic, M., Schreiber, M. R., Parsons, S. G., et al. 2016, *MNRAS*, 457, 3867
- Zucker, S., Mazeh, T., & Alexander, T. 2007, *ApJ*, 670, 1326